Analysis of the Casson and Carreau-Yasuda Non-Newtonian Blood Models in Steady and Oscillatory Flows Using the Lattice Boltzmann Method

Joshua Boyd* and James M. Buick†
Physics and Electronics, University of New England
Armidale, NSW 2351, Australia

Simon Green‡
Human Biology, University of New England
Armidale, NSW 2351, Australia
(Dated: July 23, 2007)

The lattice Boltzmann method is modified to allow the simulation of non-Newtonian shear dependent viscosity models. Casson and Carreau-Yasuda non-Newtonian blood viscosity models are implemented and are used to compare two dimensional Newtonian and non-Newtonian flows in the context of simple steady flow and oscillatory flow in straight and curved pipe geometries. It is found that compared to analogous Newtonian flows, both the Casson and Carreau-Yasuda flows exhibit significant differences in the steady flow situation. In the straight pipe oscillatory flows, both models exhibit differences in velocity and shear, with the largest differences occurring at low Reynold's and Womersley numbers. Larger differences occur for the Casson model. In the curved pipe Carreau-Yasuda model moderate differences are observed in the velocities in the central regions of the geometries, and the largest shear rate differences are observed near the geometry walls. These differences may be important for the study of atherosclerotic progression.

PACS numbers: 47.11.Qr, 47.50.-d

I. INTRODUCTION

Atherosclerotic cardiovascular disease is a leading cause of morbidity in the industrialised world [1, 2]. There is a body of evidence that suggests a correlation between atherosclerosis, regions of low blood-flow velocity, rotational flow, low and oscillatory shear stress near the walls of arteries [3–7]. The study of blood flow and it's hemodynamical properties can therefore lead to a greater understanding of atherosclerosis and its dependence on flow parameters. However, accurate measurements of quantities of interest, such as shear stress, are difficult to make *in vivo*, thus numerical simulation becomes a valuable investigative tool.

The lattice Boltzmann method (LBM) [8–10] has been developed as an alternative method for modelling fluid flows. The LBM uses a simplified kinetic equation to simulate fluid flows and has been applied to many general problems including turbulence [12], magnetohydrodynamics [13] and multiphase flows [14], as well as in areas relevant to blood flow simulation such as in flows with elastic and moving boundaries [15], steady and pulsating flow [16], particle suspensions [17] and flows with complex boundaries [18].

The LBM has also been applied to the simulation of blood flow [19–30] and has been shown to be suitable for modelling a number of features which are important to arterial hemodynamics. In general, blood is assumed to be a Newtonian fluid. It is held that this assumption is an acceptable approximation for larger vessels, such as the carotid artery [31, 32]. However, given the dependence of atherosclerosis on near wall shear, it needs to be asked whether this assumption remains valid for applications studying atherosclerotic progression.

Alternative methods are available for simulating non-Newtonian fluids [33–37], however LBM modelling of non-Newtonian blood flow is currently an active area of research due to the advantageous properties of the LBM, which include the local nature of the algorithm, which allows easy calculation of the velocity and shear, suitability to parallel implementation, and the availability of easily implemented boundary schemes which allow for the modelling of complex geometries.

Artoli *et al.* have studied the properties of non-Newtonian blood flow using LBM techniques under a limited number of parameter conditions [38–40]. This paper will examine the Newtonian blood assumption for a range of parameter conditions.

In this paper, a non-Newtonian flow model using the LBM will be presented in Section II A. It will be used to simulate steady (Section III A) and oscillatory flows in straight (section III B) and curved (Section III C) two dimensional pipes. The non-Newtonian properties of the fluid will be modelled using the Casson [34] and Carreau-Yasuda (C-Y) [41] models described in section II B. The results will be compared to analogous Newtonian flows in order to characterise the differences.

*Electronic address: Jboyd3@une.edu.au
†Electronic address: jbuick@une.edu.au
‡Electronic address: simon.green@une.edu.au

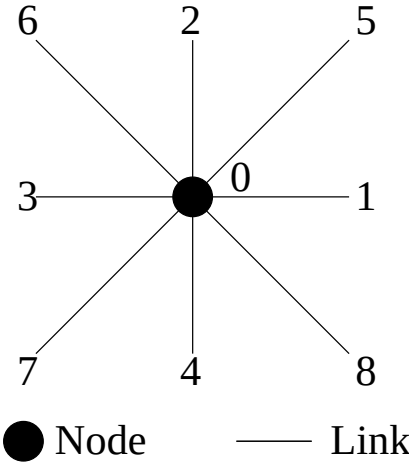

FIG. 1: The D2Q9 lattice. The black circle is the node, and the lines are the link directions, numbered from 1 to 8.

II. THEORETICAL BACKGROUND

A. The Lattice Boltzmann Method

The LBM uses a modified molecular dynamics approach to model fluid flow [8]. In the LBM, particle distribution functions, $f_i(\boldsymbol{x},t)$ at point $\boldsymbol{x}$ and time t, are confined to move synchronously on a regular lattice. The distribution functions interact on the lattice in a way that conserves mass and momentum and ensures the fluid is isotropic and Galilean invariant. Here, i labels the lattice link the distribution function is on. $(i = 0, 1 \cdots, 8)$ for the D2Q9 lattice, shown in Figure 1

The evolution of the distribution functions on the lattice is governed by the discrete Boltzmann equation [8–11]

$$f_i(\boldsymbol{x} + \boldsymbol{e}_i\Delta x, t + \Delta t) = f_i(\boldsymbol{x},t) + \Omega_i(\boldsymbol{x},t), \qquad (1)$$

where for the D2Q9 lattice, see Figure 1,

$$\begin{aligned} \boldsymbol{e}_0 &= (0,0), && (i=0), \\ \boldsymbol{e}_i &= \left(\cos\left(\tfrac{\pi}{2}(i-1)\right), \sin\left(\tfrac{\pi}{2}(i-1)\right)\right), && (i=1,2,3,4), \\ \boldsymbol{e}_i &= \sqrt{2}\left(\cos\left(\tfrac{\pi}{2}(i-1)+\tfrac{\pi}{4}\right), \sin\left(\tfrac{\pi}{2}(i-1)+\tfrac{\pi}{4}\right)\right), && (i=5,6,7,8), \end{aligned} \qquad (2)$$

and Ω_i is the collision operator. The fluid density ρ and velocity $\boldsymbol{u}$ can be calculated directly from the distribution functions at each node by

$$\rho = \sum_i f_i \qquad \text{and} \qquad \rho\boldsymbol{u} = \sum_i f_i \boldsymbol{e}_i. \qquad (3)$$

It is assumed that the distribution functions f_i can be expanded formally around a local equilibrium distribution such that

$$f_i = f_i^{eq} + \varepsilon f_i^{neq}, \qquad (4)$$

where ε is a small parameter often taken to be the Knudson number, f_i^{eq} are equilibrium distribution function and f_i^{neq} are non-equilibrium distributions functions. f_i^{eq} is selected such that

$$\sum_i f_i^{eq} = \rho \qquad \text{and} \qquad \sum_i f_i^{eq}\boldsymbol{e}_i = \rho\boldsymbol{u}, \qquad (5)$$

and it is assumed that the non-equilibrium distribution functions, f_i^{neq}, can be further expanded as

$$f_i^{neq} = f_i^{(1)} + \varepsilon f_i^{(2)} + o(\varepsilon^2), \qquad (6)$$

where

$$\sum_i f_i^{(k)} = \sum_i f_i^{(k)}\boldsymbol{e}_i = 0, \qquad k = 1,2. \qquad (7)$$

The collision operator Ω_i is given by the Bhatnagar-Gross-Krook approximation as [8–10, 13, 42, 43]

$$\Omega_i = \frac{-1}{\tau}[f_i(\boldsymbol{x},t) - f_i^{eq}(\boldsymbol{x},t)], \tag{8}$$

where τ is the relaxation time. The equilibrium form of the distribution function in two dimensions for the D2Q9 lattice is given by [9, 11]

$$f_i^{eq}(\boldsymbol{x},t) = w_i\rho(1 + 3\boldsymbol{e}_i\cdot\boldsymbol{u} + \frac{9}{2}(\boldsymbol{e}_i\cdot\boldsymbol{u})^2 - \frac{3}{2}\boldsymbol{u}^2) \tag{9}$$

where $w_0 = 4/9$, $w_i = 1/9$ for i = 1,2,3,4 and $w_i = 1/36$ for i = 5,6,7,8. The relaxation time τ is related to the viscosity η by

$$\eta = \frac{(2\tau - 1)\rho}{6}. \tag{10}$$

The LBM reproduces the Navier stokes equation in the nearly incompressible limit and is second order accurate [8–10].

The stress tensor for an incompressible fluid with pressure p is given by

$$\sigma_{\alpha\beta} = -p\delta_{\alpha\beta} + 2\eta S_{\alpha\beta}, \tag{11}$$

where $\delta_{\alpha\beta}$ is the Kronecker delta and

$$S_{\alpha\beta} = \frac{1}{2}(\nabla_\beta u_\alpha + \nabla_\alpha u_\beta) \tag{12}$$

is the strain rate tensor.

It can be shown [44] that $S_{\alpha\beta}$ can be calculated locally at each node in the LBM as

$$S_{\alpha\beta} = -\frac{3}{2\tau}\sum_i f_i^{(1)}\boldsymbol{e}_{i\alpha}\boldsymbol{e}_{i\beta}. \tag{13}$$

The $f_i^{(1)}$ terms are calculated from the non-equilibrium part of the distribution function which is usually measured during collision. Thus calculating shear in this manner is efficient since it removes the need to calculate derivatives of the velocity. Further, the shear is calculated locally, which is particularly advantageous if the LBM is being implemented in parallel. This method for implementing shear dependent non-Newtonian flows has been shown to be second order accurate for a simple power law flow [22].

B. Non-Newtonian fluid models

Two commonly used non-Newtonian blood models are the Casson model [34] and the Carreau-Yasuda model [41]. In both models we have taken the density of blood to be $\rho = 1\times10^3 kg\ m^{-3}$.

In the following discussion we denote the second invariant of the strain rate tensor as

$$D_{II} = \sum_{\alpha,\beta=1}^{l} S_{\alpha\beta}S_{\alpha\beta}, \tag{14}$$

where $l = 2$ in the case of a two dimensional model. The shear rate is then defined as

$$\dot{\gamma} = 2\sqrt{D_{II}} \tag{15}$$

1. *Casson model*

The Casson model is broadly used to describe the shear thinning behaviour of blood. In this model the apparent viscosity is given by [31, 34, 45, 46, 49]

$$\eta(\dot{\gamma}) = \frac{1}{\dot{\gamma}}\left(k_0(c) + k_1(c)\sqrt{\dot{\gamma}}\right)^2, \tag{16}$$

where $k_0(c)$ and $k_1(c)$ are functions of the hematocrit c given by [34]

$$\begin{aligned} k_0(c) &= \frac{a\beta}{ab-1}\left(\frac{k_1(c)}{\sqrt{\eta_0}} - 1\right) \qquad \text{and,} \\ k_1(c) &= \left(\frac{\eta_0}{(1-c)^{ab-1}}\right)^{\frac{1}{2}} \end{aligned} \tag{17}$$

Here, η_0 is the plasma viscosity, a, b and β are constant parameters. $k_0(c)$ and $k_1(c)$ are determined by fitting equation (16) to physical viscometric data. In this paper parameter values of $k_0(c) = 0.1937\ (Pa)^{\frac{1}{2}}$ and $k_1(c) = 0.055\ (Pa\cdot s)^{\frac{1}{2}}$ were used, obtained from Perktold *et al.* (1991) [34].

The Casson model fits empirical data quite well for shear rates of $\dot{\gamma} > 1\ s^{-1}$ [34], however, we note that $\lim_{\dot{\gamma}\to 0}\eta(\dot{\gamma}) = \infty$, and thus this model is undefined at zero shear rate. Both k_0 and k_1 are expressed in terms of hematocrit, a measurable physical quantity and themselves have physical meaning. k_0^2 can be interpreted as the yield stress for blood, and we note that $\lim_{\dot{\gamma}\to\infty}\eta(\dot{\gamma}) = k_1^2$, a limiting asymptotic viscosity.

Equation (16) can be dimensionlessly scaled and the following dimensionless number analogous to the Reynold's number can be defined

$$Re_C = \frac{u_0 L\rho}{k_1^2}, \tag{18}$$

where u_0 and L are the peak velocity and characteristic length of the system respectively.

2. Carreau-Yasuda model

The Carreau-Yasuda model for the shear thinning behaviour of blood is also commonly used in hemodynamical simulations [31, 41, 46]. In this model the apparent viscosity is given by

$$\eta(\dot{\gamma}) = \eta_\infty + (\eta_0 - \eta_\infty)\left(1 + (\lambda\dot{\gamma})^a\right)^{\frac{n-1}{a}}, \qquad (19)$$

where a, n and λ are empirically determined constant parameters. The parameters a and n are dimensionless, the parameter λ has units of s.

The main advantage of the Carreau-Yasuda model over the Casson model is that it is continuous for all $\dot{\gamma} \geq 0$. For blood $n < 1$, thus we note that $\lim_{\dot{\gamma}\to 0} \eta(\dot{\gamma}) = \eta_0$ and $\lim_{\dot{\gamma}\to\infty} \eta(\dot{\gamma}) = \eta_\infty$, indicating that at high shear rates, the fluid acts like a Newtonian fluid with viscosity η_∞, whereas at low shear rates, the fluid acts like a Newtonian fluid with viscosity η_0. The parameters a, n and λ control how the fluid behaves in the non-Newtonian regime between these two asymptotic viscosities. The continuity of this model at low shear rates allows for an easier implementation in numerical modelling schemes.

In this paper parameter values of $\eta_0 = 0.1600\ Pa\ s$, $\eta_\infty = 0.0035\ Pa\ s$, $\lambda = 8.2\ s$, $a = 0.64$ and $n = 0.2128$ were used, obtained from Abraham *et al.* (2005) [41]. The following dimensionless number analogous to the Reynold's number can also be defined

$$Re_{CY} = \frac{u_0 L \rho}{\eta_\infty}. \qquad (20)$$

III. RESULTS

Casson and Carreau-Yasuda flows were implemented in the LBM through the coupling of equation (10) with equations (16) and (19) respectively. Steady and oscillatory flow simulations were conducted and the results for the non-Newtonian flows were compared to analogous Newtonian flows. The analogous Newtonian flows were defined as having the same pressure gradient, and viscosities of $\eta = k_1^2$ for the Casson comparison and $\eta = \eta_\infty$ for the Carreau-Yasuda comparison. Boundary conditions were implemented using the extrapolation boundary scheme developed by Guo *et al.* (2002) [18] which has been shown to be second order accurate in both steady and oscillatory flows [12, 18]. For the straight pipe geometries in sections A and B the pressure gradient was implemented using a body forcing term [47]. Due to the geometry of the pipe, 2D oscillatory flow in the curved pipe of section C was driven by the pressure boundary conditions given by Inamuro *et al.* [48].

Figure 2 shows the shear thinning behaviour of the LBM non-Newtonian models as a function of the shear rate compared to the constitutive equations for the C-Y, equation (19), and Casson, equation (16), models. The relaxation parameter τ ranged between $0.5015 - 0.8457$. The LBM results for both models accurately model the shear dependent viscosity, demonstrating the suitability of the LBM for a variety of non-Newtonian flow applications.

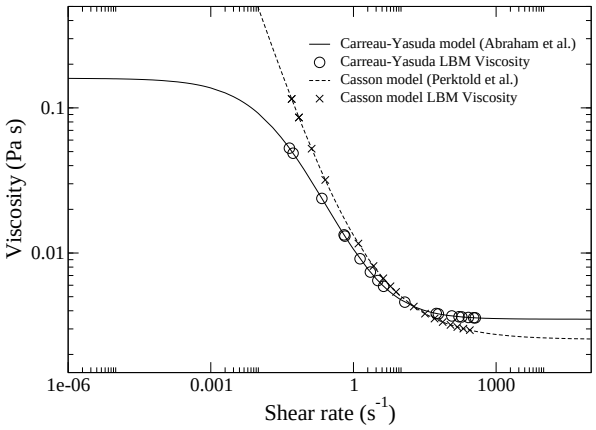

FIG. 2: Shear dependent viscosities for the Carreau-Yasuda [41] (solid line) and Casson [34] (dashed line) models compared to LBM viscosity behaviour.

A. Steady non-Newtonian flow

Steady non-Newtonian flow was implemented in a 2D pipe using the Casson [34] and Carreau-Yasuda [41] constitutive models to simulate the non-Newtonian behaviour of blood. Parameter values for the models were scaled to fit the physiological data for the human carotid artery at peak flow given in Perktold *et al.* [34]: $u_0 = 0.65\ m\ s^{-1}$ and $L = 6.2 \times 10^{-3}\ m$

Three sets of parameters were used for the non-Newtonian models. For the Casson model the parameters from Perktold *et al.* [34] were used, these parameters will be referred to as parameter set one PS_1. For the Carreau-Yasuda model, parameters from Abraham *et al.* [41] were used (PS_2). The third set of parameters (PS_3) were obtained by fitting the Casson model to the data generated from the Abraham parameters for the Carreau-Yasuda model. The PS_3 values were obtained so that a distinction could be made between the differences caused by the use of different *parameters* and the differences caused by the use of different *models*. This distinction needs to be made, as the PS_1 values were fitted to data obtained from a blood mimicking fluid [34], whereas the PS_2 were obtained from physiological measurements [41]. The influence of this fact on the results needs to be determined.

Simulations were performed in 2D rigid pipe models of diameter $L = 41$ and $L = 81$. Scaling of parameters

was performed by assuming that the peak velocity in the flow simulation was $u_0 = 0.05$, and this value was used to calculate the pressure gradient G from the analytic Newtonian solution [50].

$$u_x(y) = \frac{G}{2\eta}\left(\left(\frac{L}{2}\right)^2 - y^2\right), \qquad y \in \left[-\frac{L}{2}, \frac{L}{2}\right]. \quad (21)$$

For the PS_1 values, the following cutoff was implemented, in order to avoid numerical instability at $\dot{\gamma} = 0$

$$\eta(\dot{\gamma}) = \begin{cases} \eta_C(1), & \dot{\gamma} \leq 1, \\ \eta_C(\dot{\gamma}), & \text{otherwise}, \end{cases} \quad (22)$$

where $\eta_C(\dot{\gamma})$ indicates the apparent viscosity described by the Casson model (equation (16)).

In the case of the PS_3 values, the following cutoff was imposed

$$\eta(\dot{\gamma}) = \begin{cases} \eta_0, & \forall\ \dot{\gamma} \mid \eta_C(\dot{\gamma}) \geq \eta_0, \\ \eta_C(\dot{\gamma}), & \text{otherwise}, \end{cases}$$

where η_0 is the asymptotic viscosity of the Carreau-Yasuda model, see equation (19).

The simulations were run until the following convergence criterion was satisfied

$$\sum_{\boldsymbol{x}} \|\boldsymbol{u}(\boldsymbol{x}, t) - \boldsymbol{u}(\boldsymbol{x}, t-1)\| < \varepsilon, \quad (23)$$

where ε is a small number taken to be $\varepsilon = 1 \times 10^{-10}$. The difference between the non-Newtonian and Newtonian velocities was calculated using

$$\Delta_V = \frac{\sum_{\boldsymbol{x}} ||\boldsymbol{u}_N(x) - \boldsymbol{u}_{\bar{N}}(x)||}{\sum_{\boldsymbol{x}} ||\boldsymbol{u}_N(x)||}, \quad (24)$$

where $\boldsymbol{u}_N(x)$ and $\boldsymbol{u}_{\bar{N}}(x)$ are the Newtonian and non-Newtonian velocities respectively.

Figure 3 shows a comparison of the velocity profiles in pipes of diameter $L = 41$ (crosses) and $L = 81$ (solid line) at $Re = 100$ with the Carreau-Yasuda model implemented, velocities are given in lattice units. Negligible differences are observed. This indicates that a pipe diameter of 41 lattice units gives sufficient resolution.

Figure 4 shows the results for the three parameter sets in pipes of length $L = 41$ over a range of Reynold's numbers. These results show that significantly different flow profiles can be obtained depending on the models and parameters used. Here we see that for all Reynold's numbers the PS_1 flow shows the largest deviation. The PS_3 model shows a similar trend, although with a smaller

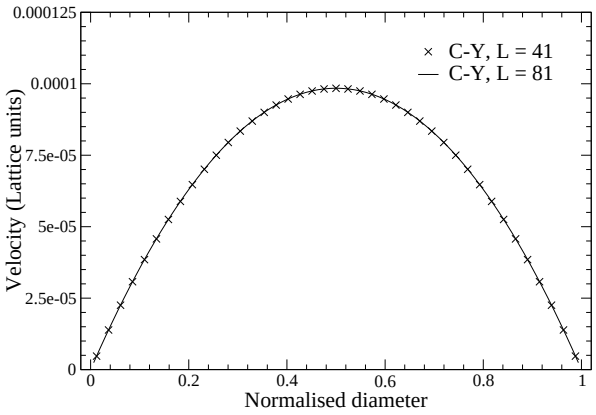

FIG. 3: Comparison of velocity profiles in pipes of length $L = 41$ (crosses) and $L = 81$ (solid line) at $Re = 100$ with the Carreau-Yasuda model implemented

overall difference for each Reynold's number. The PS_2 model shows smaller differences, and also has a steeper slope than either of PS_1 or PS_3 models, indicating that PS_1 flows profiles approach their Newtonian limit at a faster rate than the Casson models. In both cases the differences decrease for higher Reynold's numbers, which is to be expected as higher velocity flows will experience higher shear rates, causing the viscosity to approach the Newtonian limit. The different slopes of the Casson and C-Y flows results from the form of the equations used to define the non-Newtonian behaviour. The similarity between the results for the PS_2 and PS_3 models indicates that the parameters chosen for the respective models have the greatest influence on the results.

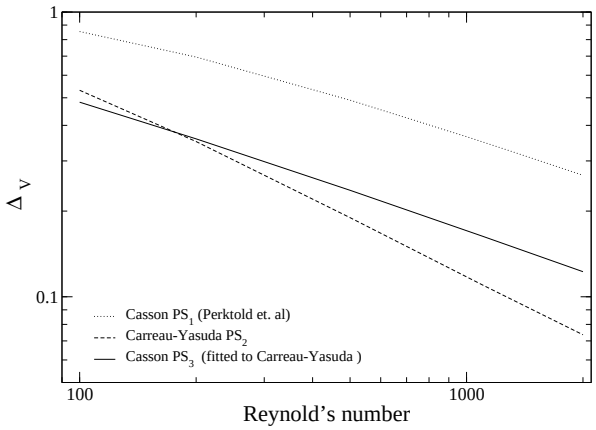

FIG. 4: Differences in velocity between Newtonian and non-Newtonian models.

Unfortunately, measuring blood viscosity is experimentally difficult and can be beset by artifacts which can

lead to inaccurate interpretations and misleading conclusions [51]. For a detailed discussion of the problems involved, please refer to Merrill [51] and Nguyen and Boger [52]. We note that the parameters from Perktold *et al.* were obtained from a blood mimicking fluid. Perktold reported no significant differences between Newtonian and non-Newtonian flows in pulsatile flow in a carotid artery geometry using the same parameters implemented in this paper. The large differences exhibited in the steady flow results presented may be due to the steady flow nature of the simulations, and further investigation is required to determine the influence of non-Newtonian flows in a physiologically accurate model.

In the next section a brief description of oscillatory flow and its implementation in the LBM shall be given. Then non-Newtonian flow in an oscillatory flow model will be examined, with the aim of further understanding differences between Newtonian and non-Newtonian flows. Flows in straight pipe will be examined.

B. Oscillatory flow: Straight pipe

2D oscillatory flow was implemented in a straight pipe geometry with the LBM using the Casson and Carreau-Yasuda models with the same parameters used for the previous steady flow simulations. If we consider a 2D oscillatory flow in a pipe of diameter L driven in the x direction by a sinusoidally varying pressure gradient of $\frac{\partial p}{\partial x} = -p^* e^{i\omega t}$, where p^* is the maximum amplitude of the pressure gradient, ω is the angular frequency of the flow and t is time, the analytic solution for velocity and shear are given by [12, 53]

$$\begin{aligned} u_x(y,t) &= \Re\left\{\frac{p^*}{i\omega\rho}\left[1-\frac{\cosh[\frac{1}{\sqrt{2}}(\alpha+i\alpha)\frac{2y}{L}]}{\cosh[\frac{1}{\sqrt{2}}(\alpha+i\alpha)]}\right]\mathrm{e}^{i\omega t}\right\}, \qquad y\in\left[-\tfrac{L}{2},\tfrac{L}{2}\right] \\ \sigma_{xy}(y,t) &= -\eta\Re\left\{\frac{2p^*}{i\omega\rho L}\cdot\frac{\sinh[\frac{1}{\sqrt{2}}(\alpha+i\alpha)\frac{2y}{L}]}{\cosh[\frac{1}{\sqrt{2}}(\alpha+i\alpha)]}\cdot\mathrm{e}^{i\omega t}\right\}, \qquad y\in\left[-\tfrac{L}{2},\tfrac{L}{2}\right]. \end{aligned} \tag{25}$$

where $\Re$ denotes the real part of the expression, ρ is the density and α is the Womersley parameter [12, 32, 54] which is defined as

$$\alpha = \frac{L}{2}\sqrt{\frac{\omega\rho}{\eta}}. \tag{26}$$

The Reynolds number for this type of flow is defined as [12]

$$\mathrm{Re}_\delta = \frac{u_0\delta\rho}{\eta} \tag{27}$$

where δ is the Stokes layer thickness, defined as [12]

$$\delta = \sqrt{\frac{2\eta}{\omega\rho}} \tag{28}$$

Simulations were run for α and Re_δ values corresponding to

$$\begin{aligned} \alpha &= 2j+1, \qquad j=0,\ldots,7 \\ Re_\delta &= 100+50j. \qquad j=0,\ldots,6, \end{aligned}$$

The behaviour of the non-Newtonian flows were compared to that of the corresponding Newtonian flows, i.e. flows with viscosities of $\eta = k_1^2$ in the Casson case and $\eta = \eta_\infty$ in the Carreau-Yasuda case, and the same pressure gradient.

All simulations were run until the following criterion was satisfied

$$\sum_{\boldsymbol{x}} \|\boldsymbol{u}(\boldsymbol{x},\kappa T) - \boldsymbol{u}(\boldsymbol{x},(\kappa-1)T)\| < \varepsilon,$$

where $\kappa \in \mathrm{N}$ and represents the number of periods that have been simulated. κ typically ranged between 10 - 200, depending on α and Re_δ. Here ε was taken to be $\varepsilon = 1\times10^{-7}$.

Once the above criterion was reached the simulation was run for one more period, during which a measure of the differences for the velocity, Δ_V, and shear, Δ_S, were calculated using the following metrics

$$\begin{aligned} \Delta_V(t) &= \tfrac{1}{N}\sum_{\boldsymbol{x}}\frac{||\boldsymbol{u}_N(\boldsymbol{x},t)-\boldsymbol{u}_{\bar{N}}(\boldsymbol{x},t)||}{||\hat{\boldsymbol{u}}_N||}, \\ \Delta_S(t) &= \tfrac{1}{N}\sum_{\boldsymbol{x}}\frac{||\boldsymbol{\sigma}_N(\boldsymbol{x},t)-\boldsymbol{\sigma}_{\bar{N}}(\boldsymbol{x},t)||}{||\hat{\boldsymbol{\sigma}}_N||}, \end{aligned} \tag{29}$$

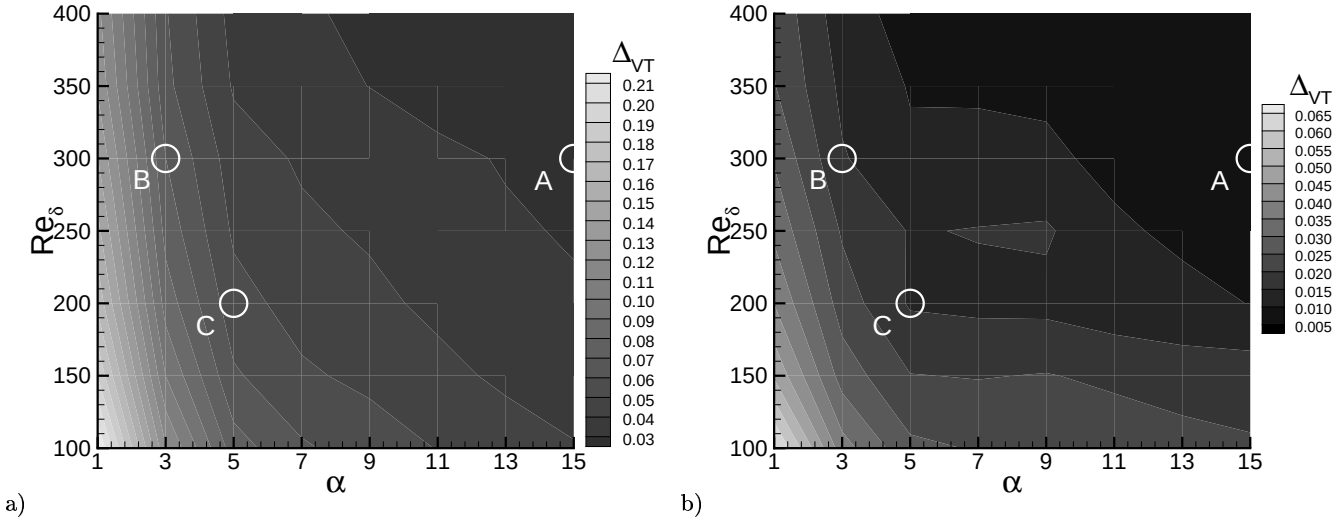

FIG. 5: Δ_{VT} for a) The Casson model, b) The Carreau-Yasuda model. The letters A, B and C indicate the α and Re_δ regions corresponding to A) The Aorta, B) The Brachial artery, C) The Carotid artery.

where $\boldsymbol{u}_N(\boldsymbol{x},t)$ and $\boldsymbol{u}_{\bar{N}}(\boldsymbol{x},t)$ are the Newtonian and non-Newtonian oscillatory velocities at time t, $\boldsymbol{\sigma}_N(\boldsymbol{x},t)$ and $\boldsymbol{\sigma}_{\bar{N}}(\boldsymbol{x},t)$ are the Newtonian and non-Newtonian σ_{xy} shear components at time t. $\hat{\boldsymbol{u}}_N$ and $\hat{\boldsymbol{\sigma}}_N$ are the peak Newtonian velocity and shear at time t. Velocities were selected at every 100^{th} of a period and N corresponds to the number of nodes in the pipe geometry.

The average differences were then defined as,

$$\begin{aligned} \Delta_{VT} &= \sum_t \frac{1}{T_n}\Delta_V(t), \text{ and,} \\ \Delta_{ST} &= \sum_t \frac{1}{T_n}\Delta_S(t), \end{aligned} \tag{30}$$

where $t \in [\kappa T, (\kappa+1)T]$ and T_n is the number of time steps included in the summation, here we use $T_n = 100$. The form of the metrics for Δ_{VT} and Δ_{ST} were chosen over that used in equation (24) due to its insensitivity to the shape of the velocity and shear profiles. This is an important property, as the shear profiles in particular, exhibit a large variation in shape depending on the Reynold's and α numbers.

The σ_{xy} component of the shear was used because from equation (25) we see that the x-component of the solution $u_x(y,t)$ for this type of flow only depends on y, and the y component $u_y(x,y,t) = 0$, thus from equation (11), $\sigma_{xx} = \sigma_{yy} = -p\delta_{\alpha\beta}$ are constant and variations in the shear rate $\dot{\gamma}$ (equation (15)) are solely determined by σ_{xy}.

Figures 5 a) and b) show the velocity results for the Casson and Carreau-Yasuda (C-Y) models respectively. The letters A, B and C and their corresponding circles indicate the general α and Re_δ regions of the aorta, brachial and carotid arteries respectively. Table I shows the parameters used to determine these arterial regions.

TABLE I: α and Re_δ values for the aorta, carotid and brachial arteries.

Artery	U_0 $(m\ s^{-1})$	Diameter (m)	α (approx.)	Re_δ (approx.)
Aorta [a]	1.09	2.54×10^{-2}	15	300
Brachial [b]	1.07	3.90×10^{-3}	3	300
Carotid [c]	0.65	6.20×10^{-3}	5	200

[a] Haugen *et al.* [57]
[b] Stoner *et al.* [56]
[c] Perktold *et al.* [34]

In both figures, the maximum Δ_{VT} are seen to occur for low α and low Re_δ. Higher differences persist for α numbers between 1-5, although this tapers off for the higher Re_δ in the C-Y case. For the higher α numbers Δ_{VT} decreases with increasing Re_δ. The graphs support the assertion that for larger arteries (Higher α and Re_δ) the assumption of Newtonian viscosity is a good first approximation [31, 32, 55], particularly for the aorta. However, the carotid artery (C) exists in a region of relatively moderate difference and the brachial artery (B) lies quite close to a region of higher difference. Thus we must question how relevant this assumption is for each of these arteries.

The scale of the errors differ greatly between the Casson and C-Y models. The Casson model shows a peak difference of 0.21, whereas the C-Y model exhibits a peak difference of 0.065, thus differing by about a factor of 3. This is also true for the minimum difference values. This large difference can be attributed directly to the different viscosity curves generated by the chosen parameters.

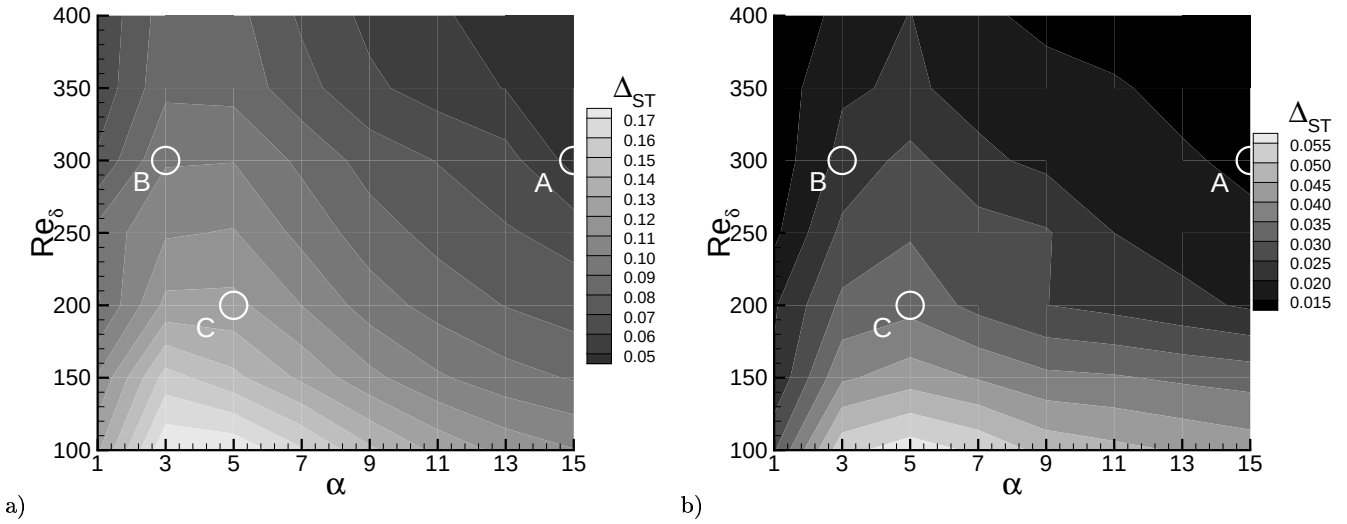

FIG. 6: Δ_{ST} for a) The Casson model, b) The Carreau-Yasuda model. The letters A, B and C indicate the α and Re_δ regions corresponding to A) The Aorta, B) The Brachial artery, C) The Carotid artery.

The C-Y model also shows more persistent higher errors for low Re_δ flows.

We also notice a large "bulge" present between $\alpha = 5$ - 9 and for $Re_\delta \geq 200$, this bulge is most prominent in Figure 5 b) for the C-Y model. This corresponds to the intermediate α region in which the velocity profile is between the characteristic parabolic (low α) and step like (large α) oscillatory profiles. The intermediate profiles exhibit tendencies of both extremes, but they notably have a dip near the center, which creates a "valley" between two "hills". Non-Newtonian flows tend to flatten the velocity profile, thus in these intermediate α regions, the valleys and hills are flattened, resulting in a more persistent difference over that range.

Figures 6 a) and b) show the shear results for the Casson and Carreau-Yasuda (C-Y) models respectively. Both these figures exhibit similar trends. In both cases Δ_{ST} decreases with increasing Re_σ for all α. For each Re we note that Δ_{ST} first increases with α, until it peaks. For the Casson model this peak is observed at approximately $\alpha = 3$, for the C-Y model the peak is observed at approximately $\alpha = 5$. Δ_{ST} decreases after this peak in all cases. These regions correspond to the α regions with high Δ_{VT}. For the Aorta, Δ_{ST} is small in both cases, but both the Brachial and Carotid arteries reside in regions of relatively higher difference.

The scale of the errors differ significantly between the two models. The Casson model shows a peak difference of 0.16, the C-Y model shows a corresponding peak difference of 0.05. This is a factor of 3 difference, similar to that seen in the corresponding velocity differences (Figure 5). Higher shear differences occur across a broader range of α in the C-Y model, A bulge similar to that seen in the velocity error graph (Figure 5) is also observed in the C-Y shear error results, for similar reasons.

As Δ_{VT} and Δ_{ST} are averaged over T, Figures 5 and 6 give us no information as to how the differences vary over the oscillation period. We would also like to know how the shear varies both over the period and between Newtonian and non-Newtonian flows.

1. *Differences over a period*

In order to observe what differences, if any, occur in the behaviour of the flows over T in a physiologically relevant manner, three specific example were been chosen. The Aorta, Brachial and Carotid arteries represent differing α and Re_δ numbers, see Table I. Table II shows the Δ_{VT} and Δ_{ST} values associated with these arteries for the Casson and C-Y models.

TABLE II: Δ_{VT} and Δ_{ST} values for Aorta, Brachial and Carotid arteries.

Artery	Model			
	Casson		Carreau-Yasuda	
	Δ_{VT}	Δ_{ST}	Δ_{VT}	Δ_{ST}
Aorta	0.0197	0.0460	0.0080	0.0139
Brachial	0.0700	0.0990	0.0154	0.0216
Carotid	0.0538	0.1230	0.0144	0.0333

In this section, the velocity and shear profiles corresponding to the Carotid artery will be examined. Figures 7 a) - d) shows comparisons between the Newtonian (solid lines) and Casson non-Newtonian (dotted lines) velocity and shear profiles for the α and Re_δ corresponding to the Carotid artery. Profiles corresponding to times of peak and low velocity were chosen to contrast the fluid behaviors at different times during the oscillation. Figures 7 a)

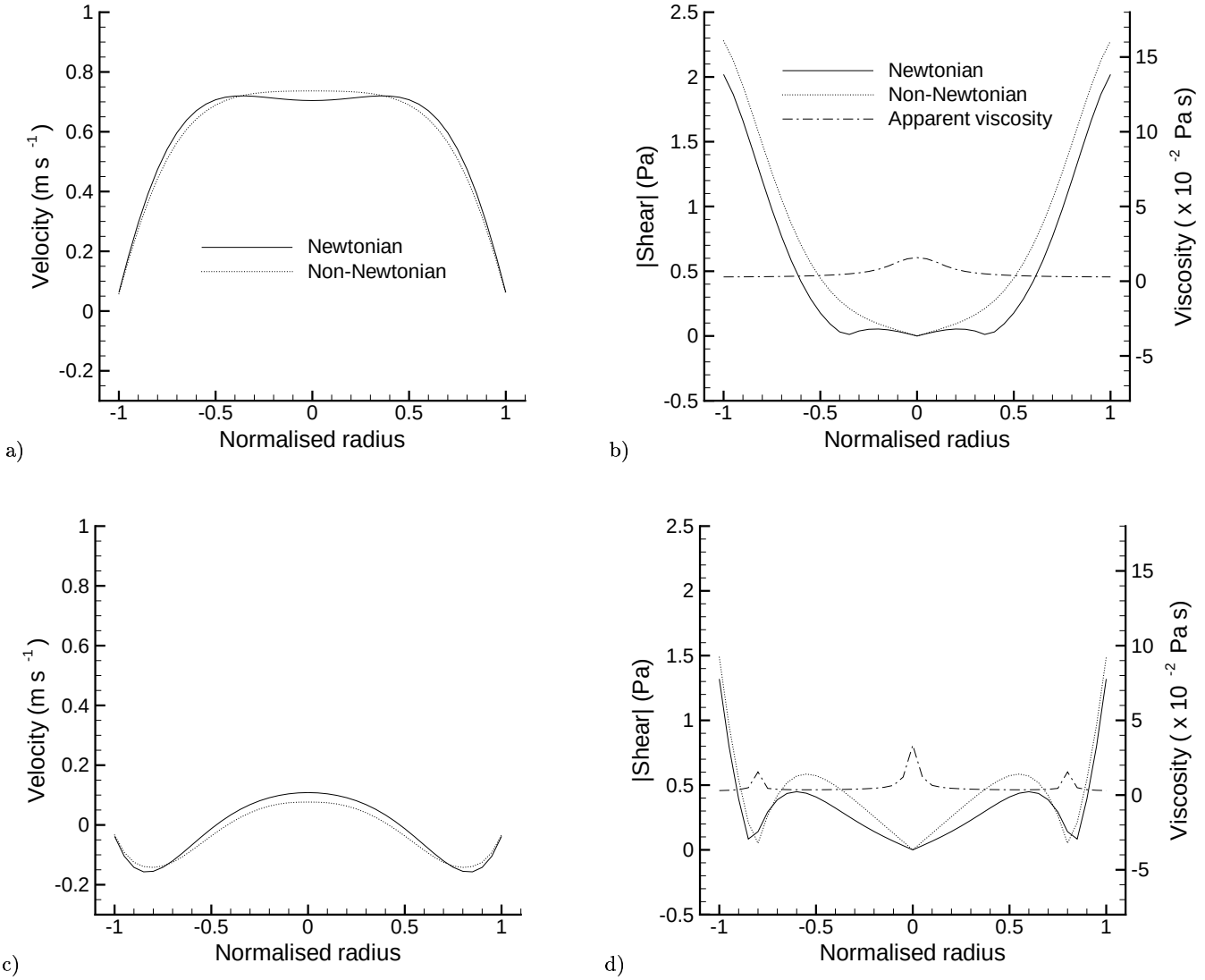

FIG. 7: Comparison of Newtonian (solid lines) and Casson non-Newtonian model (dotted lines) velocity, shear and viscosity (dot-dashed lines) profiles corresponding to the carotid artery. Profiles taken at a - b) $0.08T$ and c - d) $0.33T$.

- b) show these profile at time $t = 0.08T$, Figures 7 a) - b) show these profile at time $t = 0.33T$.

We note that for the Casson non-Newtonian model the velocity profile is flatter across the central region of the artery compared with the corresponding Newtonian model. The same flattening was observed near the edges of the profile at later times in the period (data not shown). Similar flattening was also observed in both the Aorta and Brachial artery cases. At time $t = 0.08T$ the non-Newtonian profile exhibits a larger central velocity ($0.73\ m\ s^{-1}$) than the corresponding Newtonian profile ($0.70\ m\ s^{-1}$). This phenomenon is due to the general flattening characteristic of shear thinning non-Newtonian flows, and the particular shape of the profile which is characteristic of this particular α number. After $t = 0.33T$, the non-Newtonian profile velocity is smaller in magnitude than the corresponding Newtonian flow.

Differences in the velocity profiles extend across all the pipe due to the distinct flattening in the non-Newtonian profile. These differences are largest at the peak velocity (4.4%) and lowest velocity (4.3%) timesteps.

Figures 7 b) and d) show comparisons between the Newtonian (solid lines) and Casson non-Newtonian (dotted lines) shear profiles. Differences of up to 10.5% between the Newtonian and Casson non-Newtonian profile are observed, with the predicted shears of the non-Newtonian profile being larger than the corresponding Newtonian shear. The largest differences extend across most of the pipe for the majority the period (data not shown), with the differences near the edge of the pipe becoming smaller at times corresponding to smaller velocities. The non-Newtonian shear is observed to be smaller

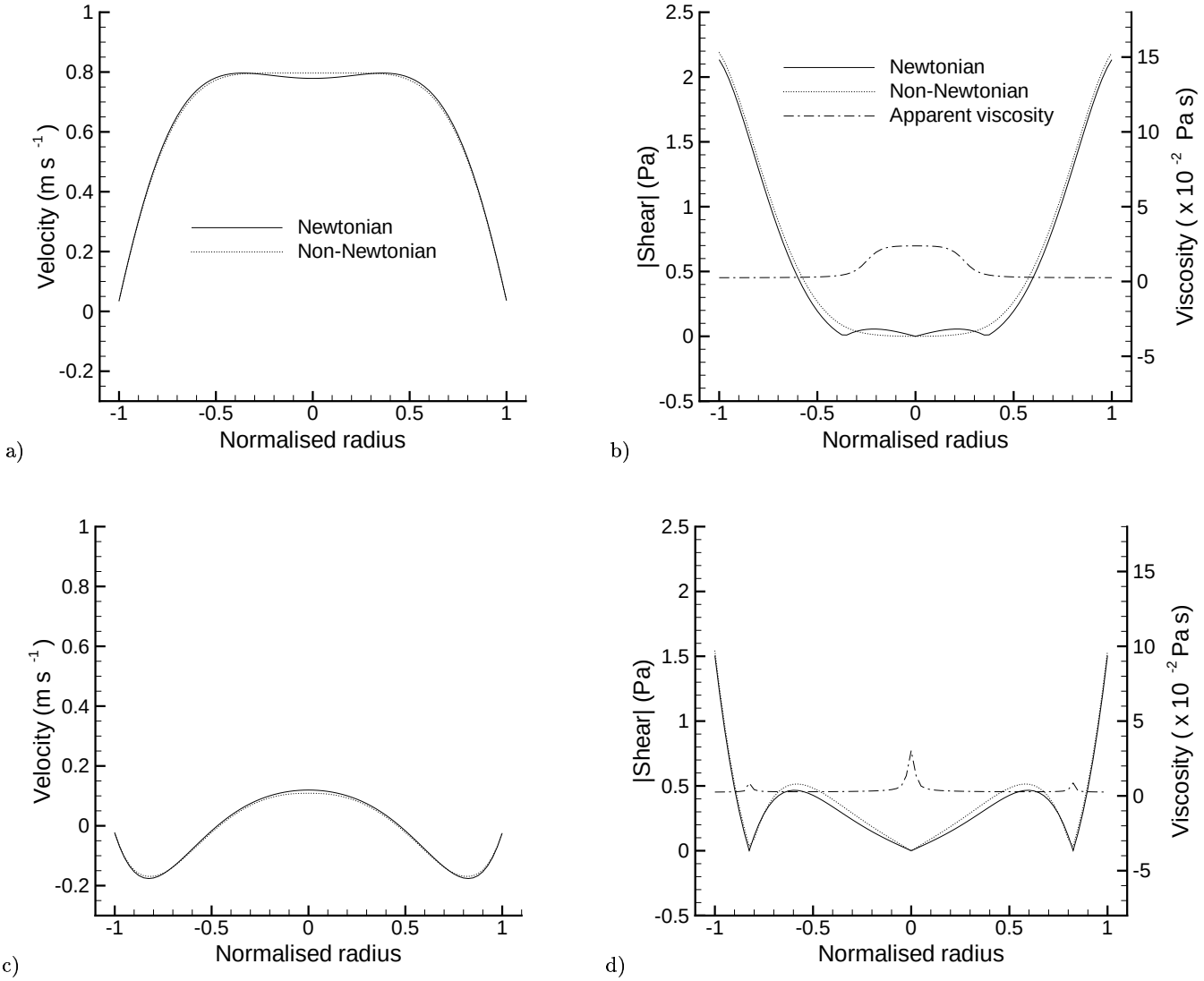

FIG. 8: Comparison of Newtonian (solid lines) and Carreau-Yasuda non-Newtonian model (dotted lines) velocity, shear and viscosity (dot-dashed lines) profiles corresponding to the carotid artery. Profiles taken at a - b) $0.08T$ and c - d) $0.33T$.

than the corresponding Newtonian shear near peaks in the apparent viscosity, Figure 7 d).

The non-Newtonian viscosity also exhibits a persistent central peak for the majority of the period and the development of two smaller peaks near the edge of the pipe at times of low velocity, Figure 7 d).

Figures 8 a) - d) shows comparisons between the Newtonian and C-Y non-Newtonian velocity profiles for the α and Re_δ corresponding to the Carotid artery. It is observed that the profiles match quite closely. The largest differences (2.2%) occur at the peak velocity, where the non-Newtonian profile flattens in a manner similar to that observed in the corresponding Casson flow. Slight flattening around the velocity minima at $t = 0.33T$ is also observed, Figure 8 d). The predicted velocities in this case are higher than those observed in the corresponding Casson case, but the differences between the Newtonian and non-Newtonian profiles are much smaller.

Figures 8 b) and f) show comparisons between shear profiles for the Newtonian and C-Y models and the apparent viscosity profile predicted by the C-Y model. We observe that the shear profiles match closely. In general the C-Y non-Newtonian shear is higher than the corresponding Newtonian shear. The largest differences (3.5%) are confined to the inner regions of the pipe, with smaller differences seen near the edge only during a relatively small proportion of the period (data not shown). Once again, the differences between Newtonian and non-Newtonian profiles are much smaller than for the corresponding Casson profiles.

The apparent viscosity profile exhibits similar behaviour to the corresponding Casson case, with a central

peak that grows for the majority of the timespan examined (data not shown). The initial peak at $t = 0.08T$ has a broader base (0.4× diameter) compared to the corresponding Casson peak (0.25× diameter). The satellite peaks in the C-Y viscosity are smaller in magnitude narrower than the corresponding Casson peaks. The magnitude of the largest peak was larger that the corresponding Casson peak (data not shown).

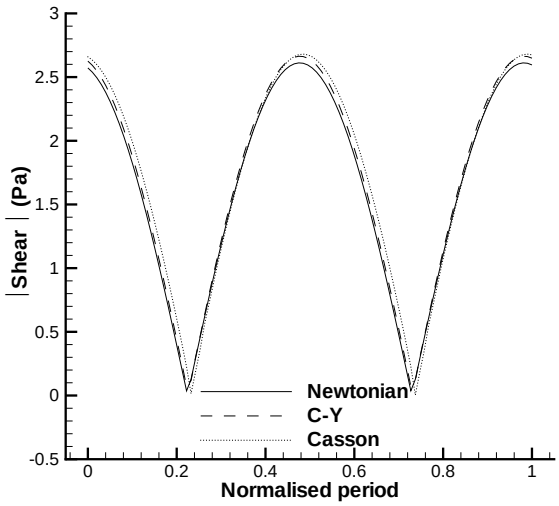

FIG. 9: Newtonian and non-Newtonian near-wall shears over one period

Figure 9 shows the near-wall shear comparison taken at half a grid-length ($0.012L$) from the wall in the Newtonian, Carreau-Yasuda and Casson oscillatory flows corresponding to the Carotid artery. The sinusoidal shear curve for the C-Y model matches that reported by Artoli *et al.* [39]. The non-Newtonian shears exhibit greater magnitudes compared to the Newtonian flow over the majority of the period for both the C-Y and Casson models, with the Casson in general showing the greatest difference. Both non-Newtonian models are also slightly phase shifted relative to the Newtonian curve. In the next section this analysis will be extended to a curved pipe geometry in order to observe the effects that complex geometries have on the flows.

C. Oscillatory flow: Curved pipe

2D oscillatory flow was implemented in the curved pipe geometry shown in figure 10 with the Carreau-Yasuda parameters used for the previous simulations.

The Reynold's number was defined from equation (20) where in this case u_0 was calculated from the pressure gradient using equation (25) as the peak velocity in a straight pipe. This u_0 may differ from the actual peak

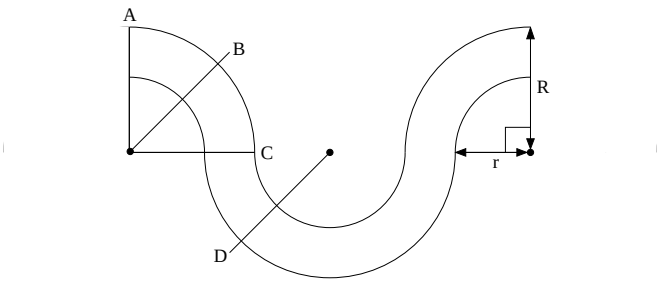

FIG. 10: Curved pipe geometry. A, B, C and D represent lines across which velocity and shear rate profiles were taken.

velocity on the curved geometry. The width of the pipe was taken to be $R-r = 40$ lattice units and the parameters were scaled accordingly. The α number was defined in the usual manner. A Reynold's number of $Re = 100$ and Womersley number of $\alpha = 1$ were used in this curved pipe simulation.

The simulations were run until the following convergence criterion was satisfied

$$\frac{1}{N}\sum_{\boldsymbol{x}} \|\boldsymbol{u}(\boldsymbol{x}, \kappa T) - \boldsymbol{u}(\boldsymbol{x}, (\kappa-1)T)\| < \varepsilon,$$

where ε was $\varepsilon = 1 \times 10^{-5}$, N was the number of fluid nodes in the geometry. κ in this case was around 40 The velocity difference was defined according to equation (29) and the shear rate difference, $\Delta_{\dot\gamma}$, was defined analogously by the equation

$$\Delta_{\dot\gamma}(t) = \frac{1}{N}\sum_{\boldsymbol{x}} \frac{||\dot\gamma_N(\boldsymbol{x}, t) - \dot\gamma_{\bar N}(\boldsymbol{x}, t)||}{||\hat{\dot\gamma}_N||}, \qquad (31)$$

where $\dot\gamma_N(\boldsymbol{x}, t)$ and $\dot\gamma_{\bar N}(\boldsymbol{x}, t)$ are the Newtonian and non-Newtonian shear rates at time t, and $\hat{\dot\gamma}_N$ in the peak Newtonian shear rate at time t. The shear rate difference was used in this section due to the curved pipe geometry. These variations are conveniently captured by the shear rate, see equation (15). Figure 11 shows a comparison of $\Delta_V(t)$ and $\Delta_{\dot\gamma}(t)$ over one period.

It can be seen that the velocity and shear differences are relatively low for the majority of the period, with peaks being seen in the regions of lowest velocity in the oscillatory period. The average differences for the velocity and shear rate were $\Delta_{VT} = 0.043$ and $\Delta_{\dot\gamma T} = 0.023$ respectively. These values are of similar order to those observed for the C-Y straight pipe oscillatory case, figures 5 and 6, although direct comparisons can not be made due to the differences in the definition of the Reynold's numbers for the two cases. In order to observe differences in the velocity and shear rate profiles spatially over the curved pipe geometry, profiles were taken across the lines A-D shown in figure 10. Profiles were taken at the times corresponding to the peak ($U_{max} = 0.4T$) and minimum ($U_{min} = 0.16T$) velocities in the curved geometry.

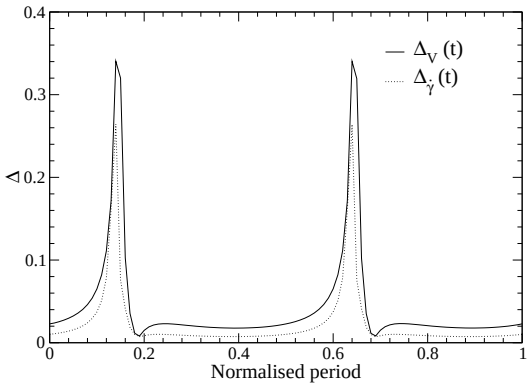

FIG. 11: Comparison of Δ_V and $\Delta_{\dot{\gamma}}(t)$ over the oscillation period.

Figures 12 a) - d) show the velocity profiles across the lines A - D respectively from figure 10. The non-Newtonian profiles show smaller peak values than the corresponding Newtonian profiles in all cases. The non-Newtonian profiles also exhibit the same flattening behaviour as was seen for the straight pipe oscillatory flow (figures 7 and 8). The largest differences are seen in the body of the flow, with only small absolute differences being seen near the walls of the geometry. A similar pattern was observed throughout the period.

Figures 13 a) - d) show the shear rate profiles across the lines A - D respectively from figure 10. The Newtonian and non-Newtonian shear rates are similar in all regions of the curved geometry. In general the Newtonian shear rate is greater than the corresponding non-Newtonian shear rate at $t = 0.4T$. At $t = 0.14T$, the non-Newtonian shear rate is slightly higher in some regions of the artery, figure 13 d). The largest differences occur in the regions near the walls of the geometry. Similar features were observed throughout the period.

IV. DISCUSSION

In the results presented many differences between Newtonian and non-Newtonian flows have been observed. In general we have seen that the predicted non-Newtonian flows are smaller in magnitude to their corresponding Newtonian flow in both steady and oscillatory flow. The exception to this trend occurs in oscillatory flow for intermediate α numbers. A particular example of this is seen in the Carotid artery for both the Casson and Carreau-Yasuda models.

For uni-directional steady flows, the differences between corresponding Newtonian and non-Newtonian profiles increase for decreasing Reynold's number. The Casson model exhibited the largest differences in both the steady and oscillatory flow cases.

Differences were also seen in the oscillatory shear profiles in the straight pipe, even for flows where the velocity profiles closely matched.The predicted shear for the non-Newtonian flows was in general higher than the corresponding Newtonian shear profiles. Differences occurred across all regions of the pipe. The non-Newtonian shear was lower than the corresponding Newtonian shear in regions of the pipe that exhibited a peak in the apparent viscosity. This phenomena occurred for both implemented non-Newtonian models.

The oscillatory velocity and shear results in the straight pipe match those reported by Artoli *et al.* [38, 39]. This paper has examined these differences over a larger parameter range and with the Casson and Carreau-Yasuda models in order to observe more general trends.

The apparent viscosity profile in the straight pipe in all cases exhibited a peak in the center of the pipe. The magnitude of this peak varied over the time period examined, increasing for $t \leq 0.23T$ and decreasing for $t \geq 0.28T$. This peak narrowed for decreasing α. Satellite peaks also occurred in all cases. The satellite peaks also varied over the period, but were in general smaller than the central peak.

The oscillatory flow in the curved geometry showed similar velocity differences to the previous flows, with the velocity profiles of the C-Y non-Newtonian flow being flattened near the center of the geometry. The shear rates in this geometry showed the greatest difference close to the walls.

We note that in figures 7 and 8 the non-Newtonian shear stress is generally greater than the Newtonian shear, as observed elsewhere [38]. This is the case even when the velocity gradient, deduced from the velocity profiles in figures 7 and 8, is seen to be smaller for the non-Newtonian case. The increased shear rate here is due to the increased apparent viscosity. In figure 13 the non-Newtonian shear rate is generally smaller than the corresponding Newtonian shear rate. This is in agreement with the velocity profiles presented in figure 12.

V. CONCLUSION

It is found that in the steady flow case both the Casson and C-Y models show large velocity differences when compared to corresponding Newtonian flows. It is observed that in all cases, steady and oscillatory, the Casson model produced the largest variations from Newtonian flow. In the steady flow situation, we observed that the parameters chosen for a particular model most affected the flow characteristics, not the model itself. The Perktold *et al.* [34] parameters used for the Casson flow were obtained from a blood mimicking fluid, whereas those of Abraham *et al.* [41] were taken from blood. Clearly these differences affect the non-Newtonian flow results.

Of particular interest is the observed shear profile differences, which were apparent even for the oscillatory Aorta case where the velocity profiles matched closely

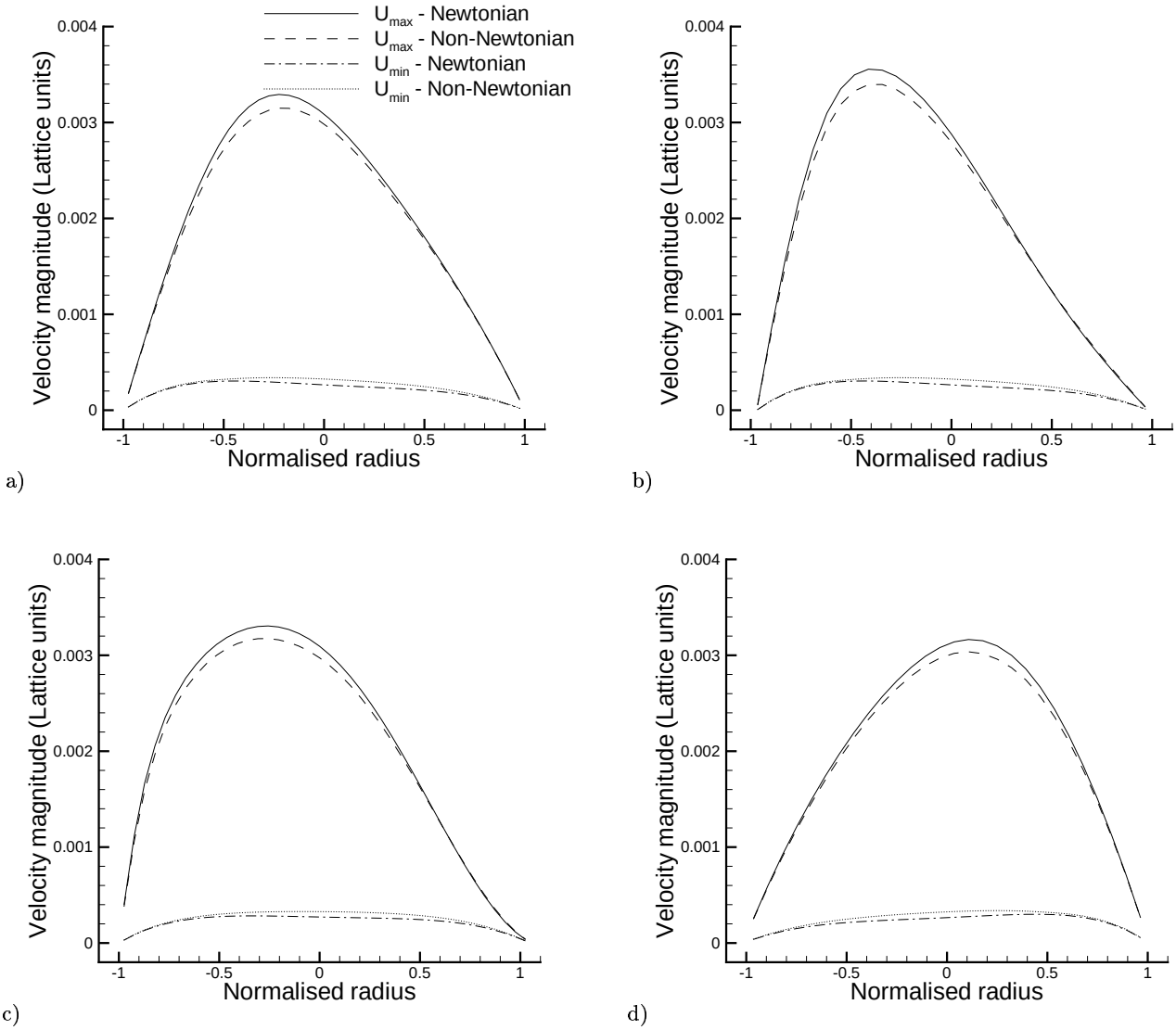

FIG. 12: Velocity profiles across lines a) A, b) B, c) C and d) D shown in figure 10. Newtonian and non-Newtonian profiles are shown at times of $t = 0.16T$ (U_{min}) and $t = 0.4T$ (U_{max}).

(data not shown). Although these differences are small, their biological implications are still uncertain. The shear rate in the curved geometry showed only small differences across the flow, indicating that geometry plays a large role in determining the non-Newtonian behaviour near the walls of a given geometry. As arterial shear rate is implicated in atherosclerotic progression, it is important that the shear behaviour of the fluid is modelled correctly. Thus the implementation of non-Newtonian flow in an accurate arterial geometry and the observation of any differences that result from using non-Newtonian and Newtonian blood viscosity models is an important next step. This will be the focus of future research.

Acknowledgments

The author would like to acknowledge that this work has been completed under the support of an Australian Postgraduate Award (APA)

[1] C. J. L. Murray and A. D. Lopez, "The global burden of disease: a comprehensive assessment of mortality and disability from diseases, injuries, and risk factors in 1990 and projected to 2020," Cambridge, (1996)

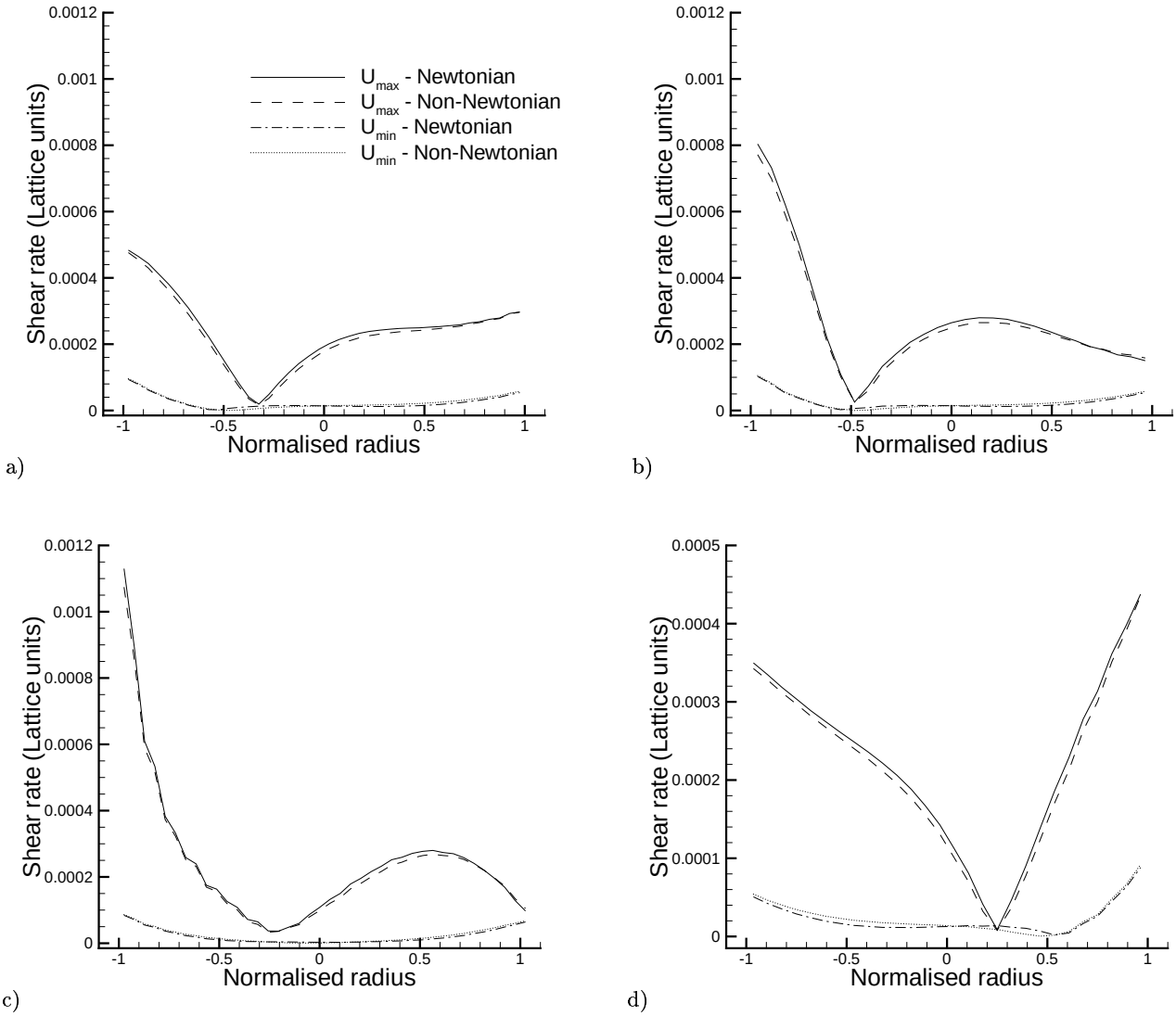

FIG. 13: Shear rate profiles across lines a) A, b) B, c) C and d) D shown in figure 10. Newtonian and non-Newtonian profiles are shown at times of $t = 0.16T$ (U_{min}) and $t = 0.4T$ (U_{max}).

[2] C. G. Caro, "Vascular fluid dynamics and vascular biology and disease," Math. Meth. Appl. Sci **24**, 1311 (2001)

[3] A. M. Malek, S. L. Alper and S. Izumo, "Hemodynamic Shear Stress and Its Role in Atherosclerosis," J. Amer. Med. Assoc. **282**, 2035 (1999)

[4] T. Asakura and T. Karino, "Flow Patterns and Spatial Distribution of Atherosclerotic Lesions in Human Coronary Arteries," Circ. Res. **66**, 1045 (1990)

[5] A. Gnasso, C. Irace, C. Carallo, M. S. De Franceschi, C. Motti, P. L. Mattioli and A. Pujia, "In Vivo Association Between Low Wall Shear Stress and Plaque in Subjects With Asymmetrical Carotid Atherosclerosis," Stroke **28**, 993 (1997)

[6] D. N. Ku, D. P. Giddens, C. K. Zarins and S. Glagov, "Pulsatile flow and atherosclerosis in the human carotid bifurcation. Positive correlation between plaque location and low oscillating shear stress," Arterioscl. Throm. Vas., **5** 293 (1985)

[7] D. C. Chappell, S. E. Varner, R. M. Nerem, R. M. Medford and R. W. Alexander, "Oscillatory Shear Stress Stimulates Adhesion Molecule Expression in Cultured Human Endothelium," Circ. Res. **82**, 532 (1998)

[8] D. A. Wolf-Gladrow, "Lattice-Gas Cellular Automata and Lattice Boltzmann Models, An introduction," Springer, (2000)

[9] S. Chen and G. D. Doolen, "Lattice Boltzmann method for fluid flows," Annu. Rev. Fluid Mech. **30**, 329 (1998)

[10] S. Succi, "The Lattice Boltzmann Equation for Fluid Dynamics and Beyond," Oxford University Press, (2001)

[11] Y. H. Qian, D. d'Humières and P. Lallemand, "Lattice BGK models for Navier-Stokes equation," Europhys. Lett. **17**, 479 (1992)

[12] J. A Cosgrove, J. M. Buick, S. J. Tonge, C. G. Munro, C. A. Greated and D. M. Campbell, "Application of the lat-

tice Boltzmann method to transition in oscillatory channel flow," J. Phys. A-Math. Gen. **36**, 2609 (2003)
[13] S. Chen, H. Chen, D. Martinez and W. Matthaeus, "Lattice Boltzmann Model for Simulation of Magnetohydrodynamics," Phys. Rev. Lett. **67**(27), 3776 (1991)
[14] X. Shan and H. Chen, "Lattice Boltzmann Model for Simulating Flows with Multiple Phases and Components," Phys. Rev. E **47**, 1815 (1993)
[15] H. Fang, Z. Wang, Z. Lin and M. Liu, "Lattice Boltzmann simulation of viscous fluid systems with elastic boundaries," Phys. Rev. E **57**(1), R25 (1998)
[16] H. Fang, Z. Wang, Z. Lin and M. Liu, "Lattice Boltzmann method for simulating the viscous flow in large distensible blood vessels," Phys. Rev. E **65**, 051925:1-11 (2002)
[17] A. J. C. Ladd and R. Verberg, "Lattice Boltzmann simulations of particle-fluid suspensions," J. Stat Phys. **104**, 1191 (2001)
[18] Z. Guo, C. Zheng and B. Shi, "An extrapolation method for boundary conditions in lattice Boltzmann method," Phys. Fluids **14**(6), 2007 (2002)
[19] M. Krafczyk, M. Cerrolaza, M. Schulz and E. Rank, "Analysis of 3D transient blood flow passing through and artificial aortic valve by Lattice-Boltzmann methods", J .Biomech **31**, 453 (1998)
[20] M. Krafczyk, J. Tölke, E. Rank and M. Schulz, "Two-dimensional simulation of the fluid-structure interaction using Lattice-Boltzmann methods," J. Comp. Struct. **79**, 2031 (2001)
[21] R. G. Belleman and P. M. A. Sloot, Proceedings of CARS 2001, "Simulated vascular reconstruction in a virtual operating theatre," 928 (2001)
[22] J. Boyd, J.M. Buick and S. Green, "A second order accurate lattice Boltzmann non-Newtonian flow model," J. Phys. A-Math. Gen. **39**, 14241 (2006)
[23] A. M. Artoli, A. G. Hoekstra and P. M. A. Sloot, Proceedings of the International Conference in Computational Science (ICCS) 2002, "Accuracy of 2D Pulsatile Flow in the Lattice Boltzmann BGK Method," 361, Amsterdam, Holland (2002)
[24] A. M. Artoli, A. G. Hoekstra and P. M. A. Sloot, "3D Pulsatile Flow With the Lattice Boltzmann BGK Method," Int. J. Mod. Phys. C **13**(8), 1119 (2002)
[25] A. M. Artoli, A. G. Hoekstra and P. M. A. Sloot, "Simulation of a systolic cycle in a realistic artery with the Lattice Boltzmann BGK method," Int. J. Mod. Phys. B, **17**(1-2), 95 (2003)
[26] J. Boyd, J.M. Buick, J.A. Cosgrove and P. Stansell, "Application of the lattice Boltzmann method to arterial flow simulation: Investigation of boundary conditions for complex arterial geometries," Australas. Phys. Eng. Sci. Med., **27**(4), 147 (2004)
[27] J. Boyd, J.M. Buick, J.A. Cosgrove and P. Stansell, "Application of the lattice Boltzmann model to simulated stenosis growth in a two-dimensional carotid artery," Phys Med Biol, **50**, 4783 (2005)
[28] R. Ouared and B. Chopard, "Lattice Boltzmann Simulations of Blood Flow: Non-Newtonian Rheology and Clotting Processes," J. Stat. Phys., **121**(1/2), 209 (2005)
[29] A. M. Artoli, A. G. Hoekstra and P. M. A. Sloot, "Mesoscopic simulations of systolic flow in the human abdominal aorta," J. Biomech. **39**(5), 873 (2006)
[30] H. B. Li, H. Fang, Z. Lin, S. X. Xu and S. Chen, "Lattice Boltzmann simulation on particle suspensions in a two-dimensional symmetric stenotic artery," Phys. Rev. E **69**(3), 031919 (2004)
[31] A. Quarteroni, M. Tuveri and A. Veneziani, "Computational vascular fluid dynamics: problems, models and methods," Computing and Visualisation in Science, **2**, 163 (2000)
[32] D. A. McDonald, "Blood Flow in Arteries," Edward Arnold (Publishers) LTD, (1960)
[33] K. Perktold, R. Peter and M. Resch, "Pulsatile non-Newtonian blood flow simulation through a bifurcation with an aneurysm," Biorheology, **26**(6) 1011 (1989)
[34] K. Perktold, M. Resch and H. Florian, "Pulsatile Non-Newtonian Flow Characteristics in a Three-Dimensional Human Carotid Bifurcation Model," J. Biomech. Eng. **113**, 464 (1991)
[35] X. Li, G. Wen and D. li, "Computer simulation of non-Newtonian flow and mass transport through coronary arterial stenosis," Appl. Msth. Mech-Engl., **22**(4) 409 (2001)
[36] P. Neofytou, "Comparison of blood rheological models for physiological flow simulation," Biorheology, **41**(6) 693 (2004)
[37] C. S. Kim, C. Kiris and D. Kwak, "Numerical Simulation of Local Blood Flow in the Carotid and Cerebral Arteries Under Altered Gravity," J. Biomech. Eng., **128**(2) 194 (2006)
[38] A. M. Artoli and A. Sequeira, "Mesoscopic Simulations of Unsteady Shear-Thinning Flows," Lect. Notes Comput. Sc., **3992**, 78 (2006)
[39] A. M. Artoli, J. Janela and A. Sequeira, "The role of the Womersley number in shear-thinning fluids," WSEAS Trans. Fluid Mech., **2**(1), Feb (2006)
[40] A. M. Artoli, J. Janela and A. Sequeira, "A comparative numerical study of a non-Newtonian blood flow model," Proceedings of the 2006 IAMSE/WSEAS International Conference on Continuum Mechanics, Chalkida, Greece, May 11-13 (2006) (pp91-96)
[41] F. Abraham, M. Behr and M. Heinkenschloss, "Shape Optimisation in Steady Blood Flow: A Numerical Study of Non-Newtonian Effects," Computer Methods in Biomechanics and Biomedical Engineering **8**(2), 127 (2005)
[42] P. L. Bhatnagar, E. P. Gross and M. Krook, "A model for collision processes in gases. I: small amplitude processes in charged and neutral one-component system," Phys. Rev. **94**, 511 (1954)
[43] S. Chen, Z. Wang, X. Shan and G. D. Doolen, "Lattice Boltzmann computational fluid dynamics in three dimensions," J. Stat. Phys. **68**, 379 (1992)
[44] A. Artoli, "Mesoscopic Computational Haemodynamics," University of Amsterdam, October (2003)
[45] A. Quarteroni and A. Veneziani, "Computational Science for the 21st Century," "Modeling and Simulation of Blood Flow Problems," Wiley (1997)
[46] F. Gijsen, "Modeling of Wall Shear Stress in Large Arteries," Eindhoven University of Technology, (1998)
[47] J. M. Buick and C. A. Greated, "Gravity in a lattice Boltzmann Model," Phys. Rev. E, **61**(5), 5307 (2000)
[48] T. Inamuro, M. Yoshino and F. Ogino, "A non-slip boundary condition for lattice Boltzmann simulations," Phys. Fluids. **7**, 2928 (1995)
[49] P. Neofytou and D. Drikakis, "Non-Newtonian flow instability in a channel with a sudden expansion," J. Non-Newton. Fluid, **111**, 127 (2003)

[50] M. C. Potter and D. C. Wiggert, "Mechanics of fluids," Prentice Hall (1991)
[51] E.W. Merrill, "Rheology of Blood," Physiol. Rev **49**(4), 863 (1969)
[52] Q.D. Nguyen and D.V. Boger, "Measuring the flow properties of yield stress fluids," Annu. Rev. Fluid Mech. **24**, 47 (1992)
[53] Engelund, F. A., "Hydrodynamik," Technical University of Denmark, (1968)
[54] J. R. Womersley, "Method for the calculation of velocity, rate of flow and viscous drag in arteries when the pressure gradient is known," J. Physiol. **127**, 553 (1955)
[55] R. L. Whitmore, "The Flow Behaviour of Blood in the Circulation," Nature, **215**, 123 (1967)
[56] L. Stoner, M. Sabatier, K. Edge and K. McCully, "Relationship between blood velocity and conduit artery diameter and the effects of smoking on vascular responsiveness," J. Appl. Physiol. **96**, 2139 (2004)
[57] B.O. Haugen, S. Berg, K.M. Brecke, H. Torp, S.A. Slørdahl, T. Skjærpe and S.O. Samstad, "Blood Flow Velocity Profiles in the Aortic Annulus: A 3-Dimensional Freehand Color Flow Doppler Imaging Study," J. Am. Soc. Echocardiog. **15**, 328 (2002)